AD_____

Award Number: W81XWH-06-1-0367

TITLE: Combined Contrast-Enhanced MRI and Fluorescence Molecular Tomography for Breast Tumor Imaging

PRINCIPAL INVESTIGATOR: Scott C. Davis

CONTRACTING ORGANIZATION: Dartmouth College
                                            Hanover, NH 03755

REPORT DATE: March 2008

TYPE OF REPORT: Annual Summary

PREPARED FOR: U.S. Army Medical Research and Materiel Command
                    Fort Detrick, Maryland 21702-5012

DISTRIBUTION STATEMENT: Approved for Public Release;
                                    Distribution Unlimited

The views, opinions and/or findings contained in this report are those of the author(s) and should not be construed as an official Department of the Army position, policy or decision unless so designated by other documentation.

REPORT DOCUMENTATION PAGE

Form Approved
OMB No. 0704-0188

Public reporting burden for this collection of information is estimated to average 1 hour per response, including the time for reviewing instructions, searching existing data sources, gathering and maintaining the data needed, and completing and reviewing this collection of information. Send comments regarding this burden estimate or any other aspect of this collection of information, including suggestions for reducing this burden to Department of Defense, Washington Headquarters Services, Directorate for Information Operations and Reports (0704-0188), 1215 Jefferson Davis Highway, Suite 1204, Arlington, VA 22202-4302. Respondents should be aware that notwithstanding any other provision of law, no person shall be subject to any penalty for failing to comply with a collection of information if it does not display a currently valid OMB control number. **PLEASE DO NOT RETURN YOUR FORM TO THE ABOVE ADDRESS.**

1. REPORT DATE	2. REPORT TYPE	3. DATES COVERED
01-03-2008	Annual Summary	15 Feb 2007 – 14 Feb 2008

4. TITLE AND SUBTITLE

Combined Contrast-Enhanced MRI and Fluorescence Molecular Tomography for Breast Tumor Imaging

5a. CONTRACT NUMBER

5b. GRANT NUMBER
W81XWH-06-1-0367

5c. PROGRAM ELEMENT NUMBER

6. AUTHOR(S)

Scott C. Davis

Email: scott.c.davsi@dartmouth.edu

5d. PROJECT NUMBER

5e. TASK NUMBER

5f. WORK UNIT NUMBER

7. PERFORMING ORGANIZATION NAME(S) AND ADDRESS(ES)

Dartmouth College
Hanover, NH 03755

8. PERFORMING ORGANIZATION REPORT NUMBER

9. SPONSORING / MONITORING AGENCY NAME(S) AND ADDRESS(ES)
U.S. Army Medical Research and Materiel Command
Fort Detrick, Maryland 21702-5012

10. SPONSOR/MONITOR'S ACRONYM(S)

11. SPONSOR/MONITOR'S REPORT NUMBER(S)

12. DISTRIBUTION / AVAILABILITY STATEMENT
Approved for Public Release; Distribution Unlimited

13. SUPPLEMENTARY NOTES
Original contains colored plates: ALL DTIC reproductions will be in black and white.

14. ABSTRACT

A unique fluorescence molecular tomography system which couples fluorescence data acquisition into the bore of a clinical MRI to image the spatial distribution of fluorescence activity in tissue volumes has been developed and characterized. Signal-to-noise and system sensitivity to fluorophore concentration have been studied extensively. In homogeneous 70mm diameter cylindrical phantoms, the system shows a linear response to fluorophore concentration down to 1nM and is sensitive down to 10pM. Images in realistic phantoms simulating breast tissue reveal the importance of the complimentary MRI information, especially in cases where the tumor to normal tissue fluorophore uptake isless than perfect. Reconstructing images using tissue morphology information from simultaneously acquired MRI images recover tumor regions down to contrasts of 1.5 to 1while images reconstructed without the MR information show no tumor specificity even at contrasts above 6 to 1.
.

15. SUBJECT TERMS
tomography, fluorescence, imaging, near-infrared, diffuse optical tomography, fluorescence molecular tomography

16. SECURITY CLASSIFICATION OF:

a. REPORT	b. ABSTRACT	c. THIS PAGE	17. LIMITATION OF ABSTRACT	18. NUMBER OF PAGES	19a. NAME OF RESPONSIBLE PERSON USAMRMC
U	U	U	UU	32	19b. TELEPHONE NUMBER *(include area code)*

Standard Form 298 (Rev. 8-98)
Prescribed by ANSI Std. Z39.18

Table of Contents

Introduction

The scientific objective of this research is to develop and characterize an MRI coupled fluorescence molecular tomography (FMT) system and associated reconstruction algorithms to image exogenous fluorescent agents in human breast. Imaging the spatial distribution of unspecific and/or targeted fluorescent probes may help determine whether a suspect region in an MRI image is indeed malignant, thus reducing the high number of false positives and associated biopsies, and aiding in treatment planning. Fluorescence imaging at depth in tissue is challenging for a number of reasons. The nature of non-invasive diffuse imaging requires detection at the tissue surface, making the data set fairly sparse compared with the volume of interest. This results in relatively poor resolution, depth dependent sensitivity, and inaccurate quantification, especially in complex tissue volumes such as human breast. Secondly, low levels of fluorescence emission are often swamped by excitation cross-talk from the exciting laser source. The FMT system here seeks to address both of these issues. Image resolution and quantification performance is addressed by incorporating the system into a clinical MRI for dual-modality image acquisition and using the MR image as a tissue structure template to guide the FMT image formation. Excitation contamination is addressed by using spectrometer-based detection systems which provide a unique opportunity to de-couple fluorescence and excitation signals using a spectral fitting routine. This report summarizes the major accomplishments through this funding period.

Body

This funding year resulted in considerable progress towards the scientific aims of this project, including the completion of comprehensive system assessment studies, demonstration of imaging progressively more complex tissue phantoms and further development of system and calibration software. Specifically, Aim 1 is answered, further evidence supporting Aim 2 is provided, Aim 3 is addressed in phantom studies and simulation studies address Aim 5. A significant fluorescence peak shift was observed for Lutex emission propagating through tissue phantoms, an unexpected result which is under investigation, as reported here.

Imaging system characterization

One of the primary accomplishments of this funding year was a comprehensive characterization of the spectrometer-based fluorescence imaging system which included methical assessments of measurement repeatability and system sensitivity to fluorescence activity. Most of the information in this section is presented in an upcoming publication[1] (attached as Appendix), though the highlights are provided here. Repeatability measurements were made for two imaging modes, one records the intensity of the excitation source while the other filters the excitation light and measures the fluorescence emission intensity. An 8.6cm diameter homogeneous phantom composed of silicone, titanium dioxide, and India ink was used to measure the repeatability of transmission mode measurements using the spectroscopy system. Optical properties of the phantom were approximately 0.004 mm^{-1} and 1.91 mm^{-1} for the absorption and reduced scattering coefficients respectively. The average and maximum standard errors are 0.28% and 0.37% for fibers remaining in contact with the phantom and 14.8% and16.3% for re-positioned fibers, indicating the larges source of error is fiber position. However, this can be addressed, as described below.

Determining measurement repeatability in fluorescence mode is less straightforward given the signal dependence on fluorophore concentration, absorption spectrum, and quantum yield. For this study, a 70 mm diameter liquid phantom containing DPBS, 1% intralipid, India ink. The fluorophore used in this study was indocayanine green (ICG), perhaps the most commonly used fluorophore for fluorescence tomography in phantoms. A concentration of 10nM ICG was used to determine measurement repeatability. Repeatability was calculated in two ways, one considered only the raw data for a given binned pixel array and resulted in a mean standard error of 0.7% and maximum standard error of 1.4% for the pixel array at the fluorescence peak. The second measure was determined based on the integrated intensity from the full calibration and spectral fitting

routine, resulting in an average standard error of 0.6% and maximum standard error of 1.8%. It is clear that fiber positioning variability would dominate the data error for fluorescence measurements in this case. However, fluorescence measurement data offers a unique opportunity to account for fiber coupling variability by calibrating the fluorescence measurements to the transmission measurements in the same geometry. This provides inherent stability to systematic error.

A 70 mm diameter liquid phantom containing DPBS, 1% intralipid and India ink was used to investigate the overall sensitivity of the system to ICG fluorescence. Optical properties at the excitation and emission wavelengths were recovered for each concentration of ICG from data collected using the clinical frequency domain system. Since the domain was known to be homogeneous, these 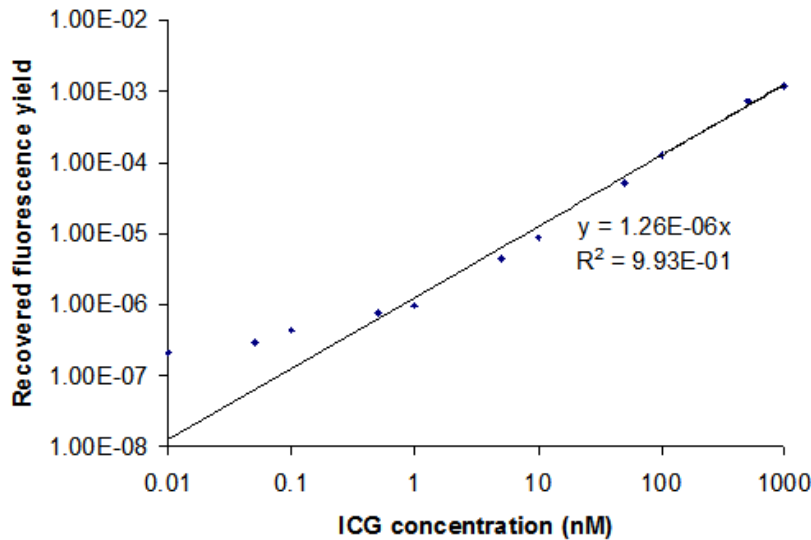properties were determined in a homogeneous fitting procedure only. Values of fluorescence yield recovered are plotted as a function of known ICG concentration in Fig. 1. The linear fit shown in the figure indicates a strong linear correlation of recovered fluorescence yield and ICG concentration (R^2 = 0.99). At 1nM, the residual between the recovered value of fluorescence yield and the linear approximation is 0.4%. As the fluorophore concentration drops below 1nM, there is a loss of the consistent linear response observed at higher concentrations. At 500pM, the residual increases to 57%, however, there is still modest sensitivity to changes in fluorophore

The linear fit equation shown: $y = 1.26\text{E-}06x$, $R^2 = 9.93\text{E-}01$

Fig. 1. Recovered values of fluorescence yield as a function of ICG concentration in a 70mm liquid phantom. Values were determined using a homogeneous fitting algorithm for the background optical properties as well as the fluorescence yield.

concentration down to the lowest concentration, 10pM. It should be noted that since fluorophore quantum yield is not explicitly known in this solution, the calculated slope of the linear regression does not provide information on the actual relationship between true and recovered concentration, however, the linearity itself is a critical measure of system performance.

Imaging clinically relevant volumes
Funding year 2006-2006 resulted in a series of phantom images of fluorescence yield in cases where perfect drug uptake is assumed. These studies provided an initial feasibility validation, however, perfect uptake experimental conditions are unrealistic for clinical applications since even targeted drugs are expected to produce background signals in healthy tissue regions. In this report, images of clinically relevant breast-sized tissue volumes were produced showing recovered images of low contrast fluorescence activity.

92mm diameter cylindrical liquid phantoms composed of DPBS, 1% intralipid, and India ink were used to investigate the imaging sensitivity for cases of imperfect drug uptake. A 22mm diameter cylindrical plastic tube was suspended in the larger phantom volume to simulate a tumor region of elevated fluorophore concentration, as shown in Fig 2. The background liquid contained 300nM of ICG while the tumor region was composed of the same intralipid solution but with varying concentrations of the fluorophore, to produce a range of tumor to background fluorophore concentrations between 6.6:1 to 1.5:1, or 560% to 50% contrast,

respectively. Images were produced using two reconstruction techniques. One technique assumes only the outer boundary of the domain is known while the other assumes complimentary information from MRI provides the internal tissue morphology. This is the "spatial priors" reconstruction technique discussed at length in the previous year's report.

Reconstructed images using both techniques are shown in Fig. 2. It is clear that in this relatively large domain with imperfect drug uptake, reconstructing images without the tissue morphology information produces qualitatively inaccurate and misleading images. The tumor region is not qualitatively or quantitatively recovered even at the higher contrast levels. The spatial priors technique, on the other hand, essentially reduces the imaging problem from one of both localization and quantification to one of quantification only since the boundaries of the tumor are specified by the MR image. In this case, the tumor region is clearly visible in the image, even down to the lowest contrasts of 50%. The improvement provided by the spatially guided reconstruction is even more dramatic for cases of imperfect uptake, presented here, than for infinite contrast cases presented in the previous year's report. This is an important result since in vivo concentrations will likely be closer to those used in this study.
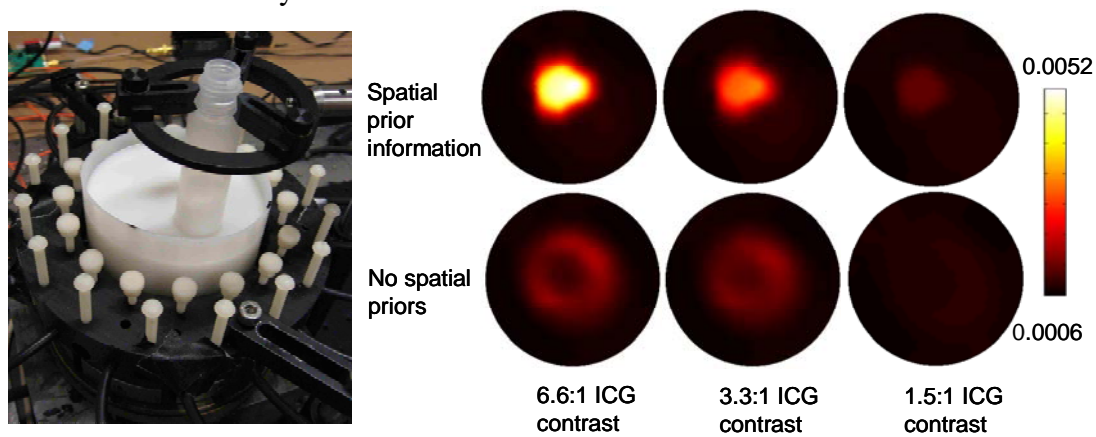

Fig. 2. A liquid tissue phantom containing simulated tumor region is pictured at left. Reconstructed images using the spatial priors approach and non-spatial priors approach for a range of ICG contrast demonstrate the advantage of using spatial guidance.

Despite the added difficulty of imaging imperfect drug uptake, the phantoms used above are still relatively simple compared to the heterogeneous structure of breast tissue. Optically, the organ can be considered as a composition of a small number of optically significant tissue types; adipose tissue, fibro-glandular tissue, and suspect regions (benign and malignant tumors, cysts). In order to investigate the imaging capabilities of the fluorescence tomography system in heterogeneous imaging volumes, a more complex phantom was created using gelatin. The 91mm diameter cylindrical phantom was composed of water, gelatin, TiO_2 for scattering, and ICG. The resulting phantom is pictured in Fig. 3 which shows the three layers; the outer layer represents adipose tissue, the second layer fibroglandular tissue, and the small cylindrical inclusion is the simulated tumor region. ICG concentrations provide a tumor to adipose contrast of 10 to 1 and a tumor to fibroglandular contrast of around 3.3 to 1. Gadolinium was also added to the second layer so that each simulated tissue region would be discernable an MRI scan for use as spatial prior information. MRI and optical data were collected and the MR images segmented to provide spatial guidance, also known as the L-matrix technique, of the fluorescence reconstructions. Resulting images are shown in Fig 3 for the spatially guided and unguided reconstructions. As is clear from the images, spatial information is critical in obtaining accurate images in complex domains.
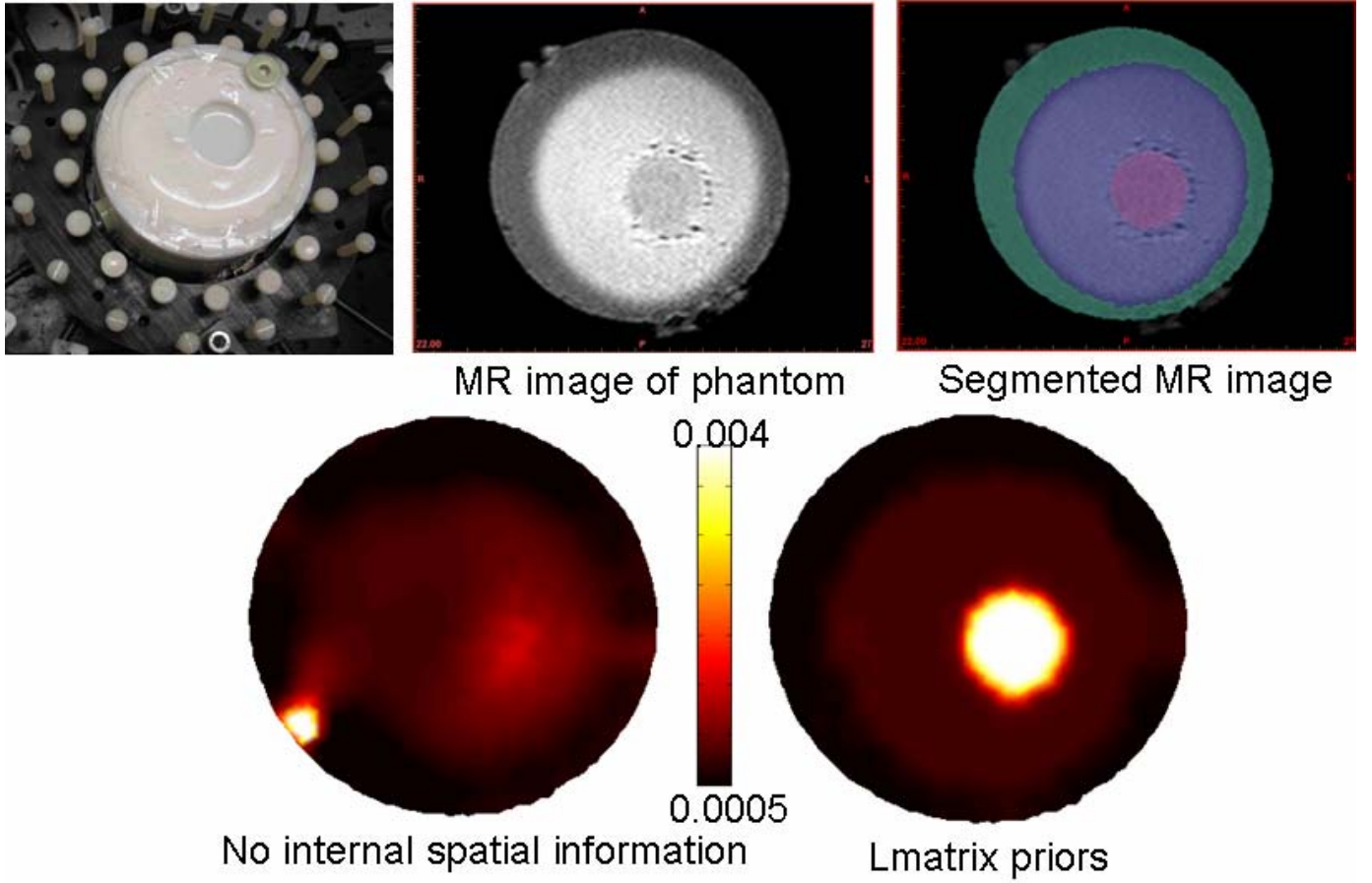
Fig. 3. Imaging a complex, 3 layer tissue simulating phantom. The top row shows a photo of the phantom, an MR image of the phantom and the MRI segmentation used in the FMT reconstruction. FMT images with and without the MRI segmentation are shown on the bottom row.

Comparing single wavelength absorption and fluorescence imaging

This study addresses the question which optical property provides the best opportunity for imaging exogenous optical contrast directly by comparing the intensity perturbation of boundary data caused by the presence of an exogenous absorber to that caused by an exogenous fluorophore. We seek to extend the analysis presented by other researchers[2] to more complex domains. A breast-shaped domain derived from an MRI scan provides the imaging test field for this simulation study. The "background" domain contains no tumor region and presents endogenous chromophore contrast only between the fatty and fibro-glandular regions, as shown in Fig. 4. Also represented in the study are two different tumor-to-normal drug uptake situations, one an idealized case with infinite contrast (Fig. 4(a)), and the other a more realistic drug uptake case resulting in finite contrast (ranging from 2:1 to 3:1) in drug concentration (Fig. 4(b)). In both cases exogenous absorption and fluorescence contrast was introduced as a simulated drug with absorbing properties of Lutex. Fluorescence quantum yield was varied as an independent variable for the fluorescence emission measurements.

The parameter of interest in this study is the relative perturbation in boundary data intensity caused by a drug-enhanced tumor. Data from perturbations caused only by exogenous *absorption* are termed "transmission" measurements, for which 735 nm was used as the laser source wavelength. Fluorescence data was generated for excitation and emission wavelengths of 690 and 761 nm and the fluorescence
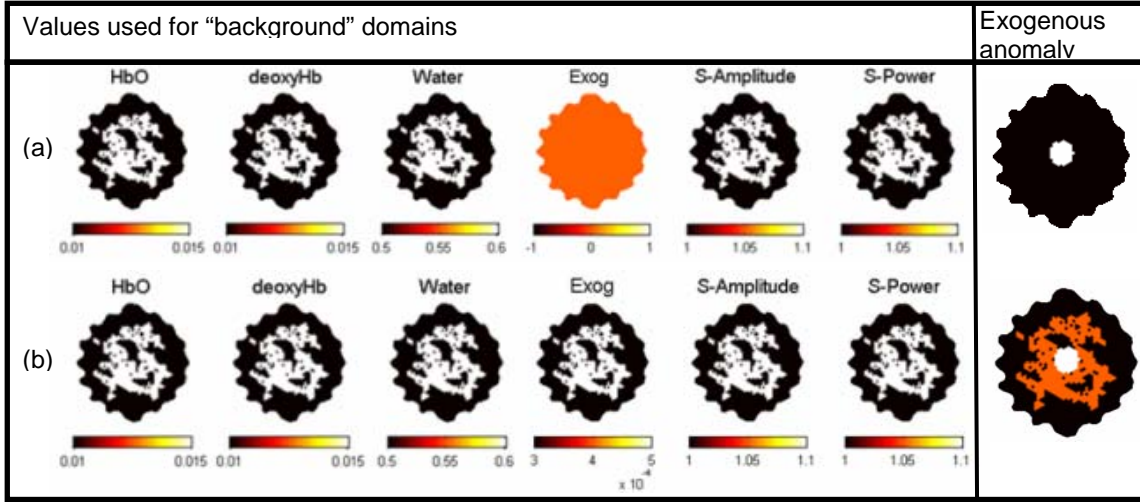
Fig. 4. Two test domains for investigating perturbations caused by absorption and fluorescence exogenous contrast. In (a), exogenous contrast tumor specificity is assumed to be perfect, while in (b), the uptake profile is more realistic.

emission perturbation was recorded as a function of fluorescence quantum yield for excitation filtering efficiencies of 3 OD, 5 OD and 7 OD. Perturbation values were calculated for three detector positions relative to a single source, as shown in Fig. 5, for both transmission and fluorescence measurements.
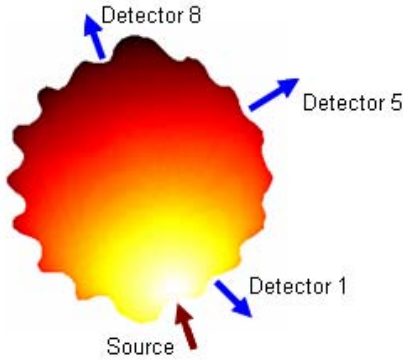

Fig. 5. Source-detector configuration used in the perturbation study.

Fig. 6 presents graphs of relative intensity perturbation as a function of fluorescence quantum yield at three detector positions for infinite exogenous agent contrast, corresponding to the test domain in Fig.(a). The graphs include perturbations of transmission intensity resulting only from an increase in the concentration of the exogenous agent as well as fluorescence emission intensity degraded by different amounts of excitation bleed-through. The perturbation caused by absorption is unaffected by quantum yield while perturbations in fluorescence signals are proportional to quantum yield.

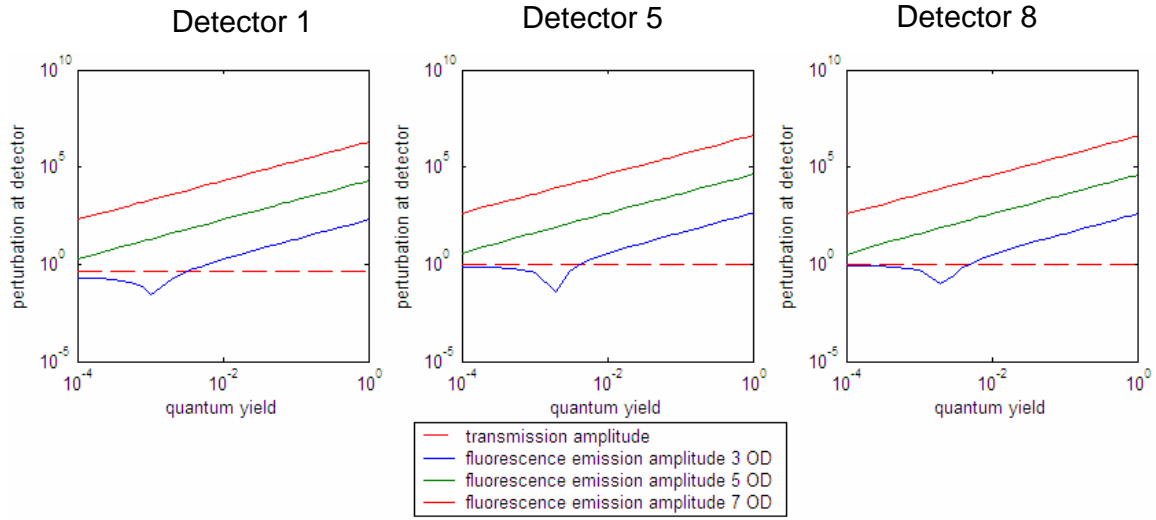It is clear from Fig. 6 that if the tissue contains infinite tumor-to-background contrast of exogenous agent concentration the fluorescence signal is more sensitive to the presence of the drug within the imaging domain. This is consistent for all source-detector pairs and filtering efficiency of 5 OD and higher given quantum yields of 0.0001 and above. These results substantiate a conclusion favoring fluorescence imaging, however, many contrast agents, including all optical agents currently approved for in vivo human use, will not provide infinite specificity and imperfect uptake must also be considered.

Fig. 6. Perturbations in transmission amplitude and fluorescence amplitude, given different filtering efficiencies and quantum yield values, caused by a centrally located object with perfect drug uptake. Under these conditions, fluorescence signals appear to be more sensitive to the object.

Figure 7 provides results for the case with drug uptake of 2:1 for tumor-to-fibro-glandular tissue layer and 3:1 for tumor-to-fatty tissue. For this case, the absorption perturbation is shown to be more significant for all values of quantum yield and filtering efficiencies tested. Significantly, these values represent the maximum expected perturbation for fluorescent anomalies and are significantly lower than perturbations caused by the absorption profile of the exogenous drug.
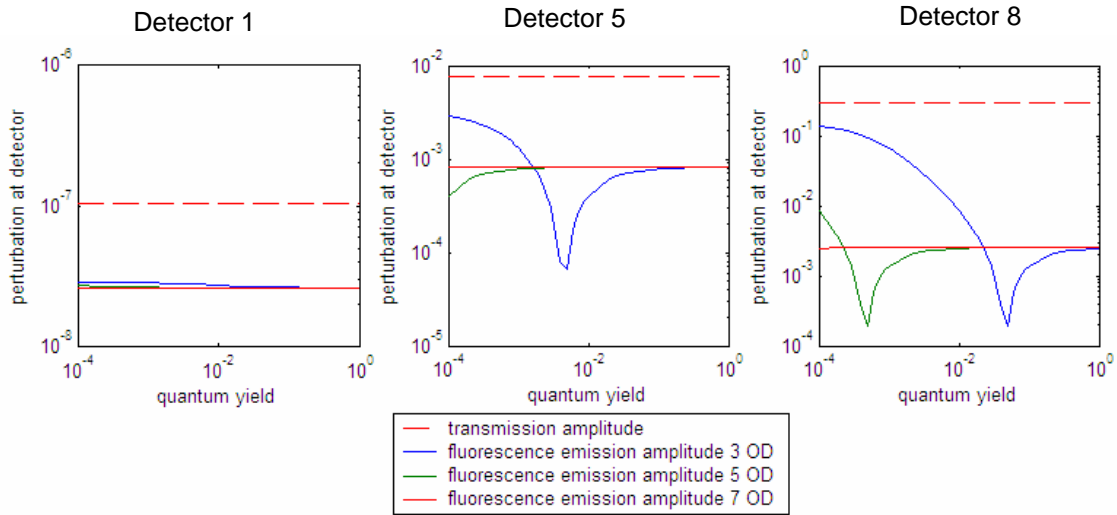

Fig. 7. Perturbations in transmission amplitude and fluorescence amplitude, given different filtering efficiencies and quantum yield values, caused by a centrally located object with imperfect drug uptake. For this lower drug contrast case, absorption measurements are more sensitive to the object than fluorescence emission, regardless of fluorescence quantum yield.

LuTex fluorescence emission peak shift in turbid phantoms

A dramatic fluorescence emission peak shift dependent on source-detector distance was an unexpected result observed in homogenous phantoms containing lutetium texaphyrin, as shown in Fig 8. One hypothesis for the apparent peak shift is the influence of the medium's wavelength dependent absorption on the propagating emission photons. Namely, shorter emission wavelengths may be preferentially absorbed by chromophores in the phantom, including the drug itself. This is consistent with previously reported behavior of emission in

turbid media[3, 4]. This was investigated by modeling the fluorescence emission spectrum as it propagates through a a homogeneous circular geometry mimicking the one used in the phantom experiments. The spectrum of Lutex, recorded in DI water, was incorporated into the model by introducing a wavelength-dependent quantum yield to imitate the shape of the emission spectrum. The absorption properties of the tissue also change with wavelength due to the absorbance spectra of the dominant chromophores. In this case, the chromophores included in the model are water and Lutex, to approximate the experimental conditions of the phantom. Assuming a 690 nm excitation source, forward models were run at discrete wavelengths within the range of the simulated emission spectrum of Lutex, thus generating intensity spectra for each source-detector pair. A selection of these spectra is shown in Fig. 9. The graphs show a dramatic change in emission spectrum profile as the emitted light propagates through the tissue. This shift is caused solely by the wavelength dependent absorption of the simulated phantom. Significantly, the emission peak settles at about 820nm for the larger source-detector distances, within nanometers of the peak observed in turbid phantoms. The simulated behavior of spectra recorded for near-source detectors does not match the experimental data, however, it should be noted that the bleed-through signal was not added to the simulated data and near-source detectors may not fall fully in the diffusion regime given the experimental parameters of this study. However, the simulated data does provide sufficient evidence to conclude that
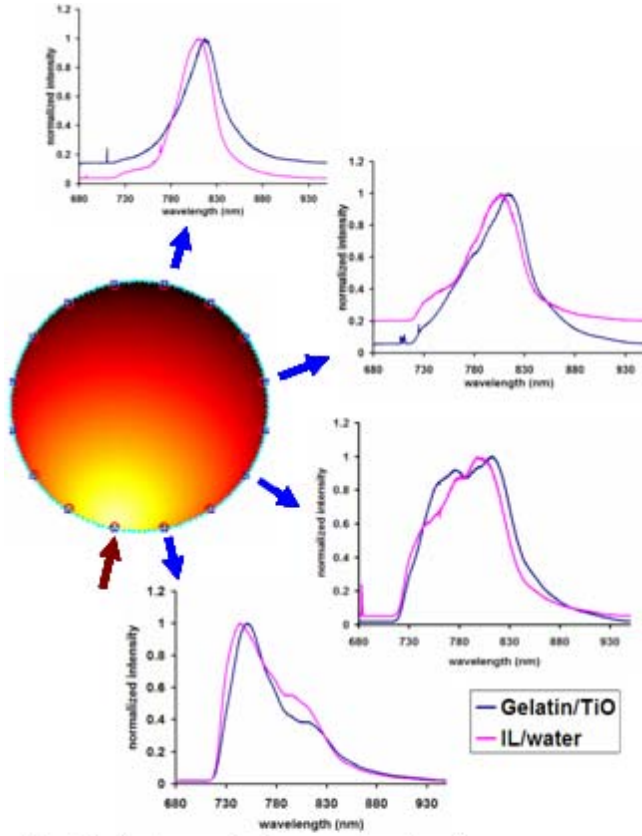

Fig. 8. Lutex emission spectra at various source-detector locations in two homogeneous phantoms, one composed of intralipid and water, and the other gelatin and TiO. Similar peak-shifting behavior is seen in both phantoms.

1) the absorption spectrum of the tissue dramatically impacts the emission spectrum propagating through tissue, 2) this effect is emphasized as the photon path-length increases, and 3) it is probable that this causes the observed peak shift phenomenon in phantoms. Such a dramatic effect offers a unique opportunity to improve the quantification of fluorescence activity by using spectrally resolved data of the fluorescence emission in the reconstruction algorithm. This approach is discussed in the proposed work section.
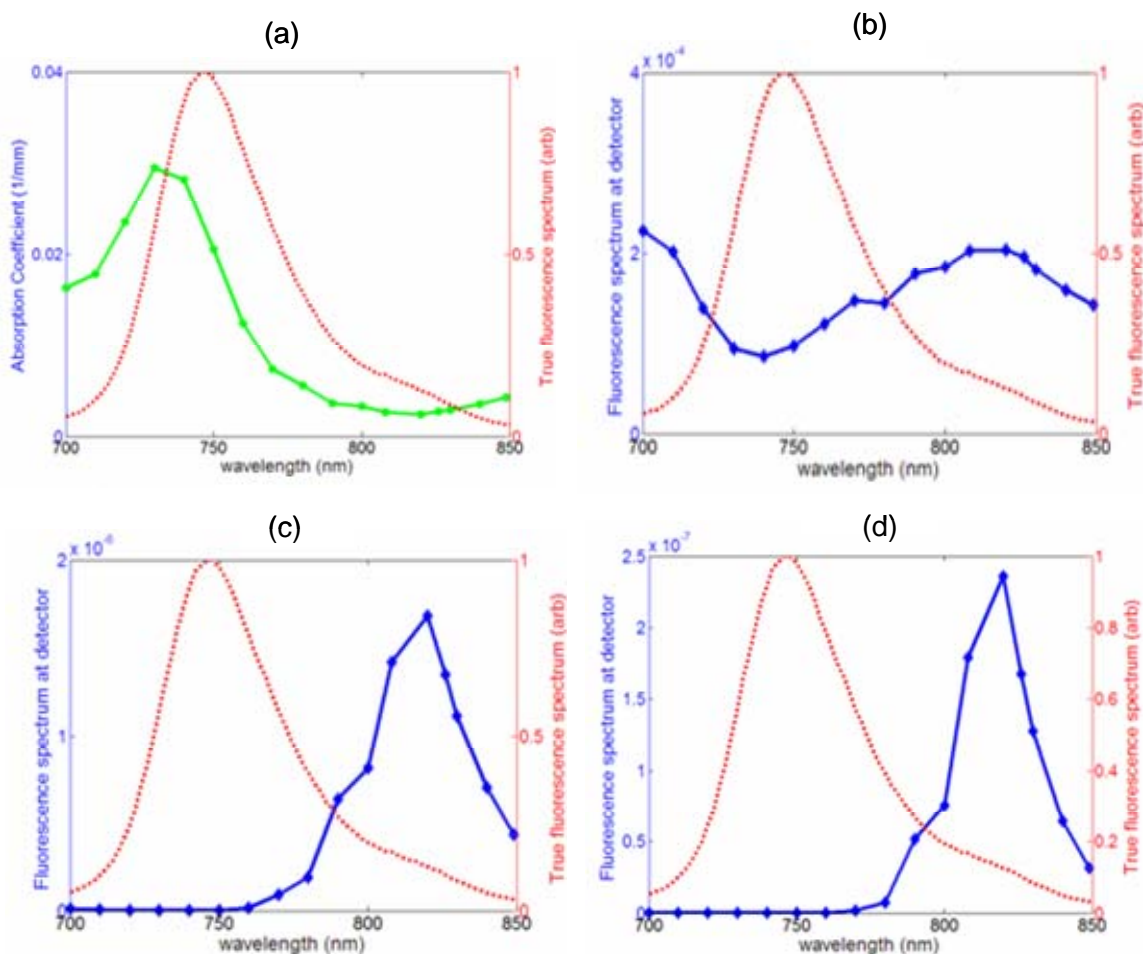
Fig. 9. The influence of absorption on the shape of an the LuTex emission spectrum. The overall absorption profile of the homogeneous simulated domain is shown in (a) (solid line), along with the unabsorbed, or true, LuTex emission spectrum (dotted line). This shape changes dramatically as it propagates through the tissue, demonstrated by (b), (c), and (d), representing the spectrum at detector positions 1, 4, and 8 respectively.

Key research accomplishments

- Completed comprehensive system performance studies to determine signal-to-noise and sensitivity to contrast agent concentration characteristics.
- Produced images of fluorescence yield in breast-sized phantoms with imperfect drug uptake.
- Continued development of experimental imaging system including calibration.
- Compared measurement sensitivity to contrasts arising from optical absorption and fluorescence signals in simulated breast domains.
- Observed fluorescence emission peak shift propagating through turbid media and developed software to model phenomenon.

Reportable outcomes

The second year of this traineeship grant led to one first author publication manuscript currently under review, another in preparation, and one first author conference presentation.

Davis SC, Pogue BW, Tuttle S, Dehghani H, Paulsen KD, *Luminescence Peak Distortion in Diffuse Molecular Spectroscopy of Tissue* (In preparation for Journal of Applied Physics, 2008).

Davis SC, Springett R, Leussler C, Mazurkewitz P, Tuttle S, Gibbs-Strauss SL, Jiang S, Dehghani H, Pogue BW, Paulsen KD, *Magnetic resonance-coupled fluorescence tomography scanner for molecular imaging of small animals and human breast* (Submitted to Review of Scientific Instruments, 2007).

Davis SC; Gibbs-Strauss SL; Tuttle S; Shudong Jiang; Springett R; Dehghani H; Pogue BW; Paulsen KD *MRI-coupled spectrally-resolved fluorescence tomography for in vivo imaging*, International Society for Optical Engineering (SPIE) BiOS-2008 at Photonics West-2008, San Jose, California, January 19-24, 2008.

Additional publications and conference proceedings references are listed below.

Wang J, **Davis SC,** Srinivasan S, Jiang S, Pogue BW Paulsen KD, *Spectral Tomography with Diffuse Near-Infrared Light: Inclusion of Broadband Frequency-Domain Spectral Data,* Journal of Biomedical Optics (In press).

Gibbs-Strauss SL, **Davis SC**, O'Hara JA, Hoopes PJ, Hasan T, Pogue BW. *MR-Guided Fluorescence Imaging of Murine Glioma Epidermal Growth Factor Uptake for Monitoring of Erbitux Therapy* (In preparation, 2007).

Gibbs-Strauss SL; **Davis SC**; A. O'Hara J; Hoopes JP; Hasan T; Pogue BW *Noninvasive murine glioma detection improved following photobleaching of skin PpIX fluorescence,* International Society for Optical Engineering (SPIE) BiOS-2008 at Photonics West-2008, San Jose, California, January 19-24, 2008.

Pogue BW, Zhiqiu L, Carpenter C, Laughney A, Krishnaswamy A, **Davis SC**; Jiang S, Paulsen KD, *System design for spectrally encoded video-rate near infrared tomography during magnetic resonance imaging of the breast,* International Society for Optical Engineering (SPIE) BiOS-2008 at Photonics West-2008, San Jose, California, January 19-24, 2008.

Conclusions

The funding period covered by this report has produced comprehensive assessments of some of the critical parameters of the FMT system. Results using this system demonstrate a linear response to fluorophore concentration down to 1nM in 70mm cylindrical phantoms. Importantly images were produces of complex phantoms simulating relatively low tumor to normal tissue contrasts, i.e., poor drug specificity, using spatially guided reconstruction techniques available only to systems incorporating into clinical imaging modalities which provide morphological information of the breast tissue. Simulation studies of realistic breast domains compared perturbations caused by changes in fluorescence and absorption signals arising from tumor uptake of a fluorescent or absorbing optical agent. Preliminary results indicate specificity is a major factor in which optical signal provides the stronger data response. Finally, an observed fluorescence peak shift in turbid media was modeled numerically. Preliminary results indicate the selective absorption of the media gives rise to the apparent shift.

References

1.   S. C. Davis, B. W. Pogue, R. Springett, C. Leussler, P. Mazurkewitz, S. B. Tuttle, S. L. Gibbs-Strauss, S. S. Jiang, H. Dehghani, and K. D. Paulsen, "Magnetic resonance-coupled fluorescence tomography scanner for molecular imaging of tissue," Rev. Sci. Instr. **(submitted)** (2008).

2.   X. Li, B. Chance, and A. G. Yodh, "Fluorescent heterogeneities in turbid media: limits for detection, characterization, and comparison with absorption," Applied Optics **37**, 6833-6844 (1998).
3.   J. Svensson, and S. Andersson-Engels, "Modeling of spectral changes for depth localization of fluroescent inclusion," Opt. Exp. **13**, 4263-4274 (2005).
4.   J. Swartling, J. Svensson, D. Bengtsson, K. Terike, and S. Andersson-Engels, "Fluorescence spectra provide information on the depth of fluorescent lesions in tissue," Appl. Opt. **44**, 1934-1941 (2005).

Appendix

The relevant journal article manuscript has been attached.

Magnetic resonance-coupled fluorescence tomography scanner for molecular imaging of tissue

Scott C. Davis[1], Brian W. Pogue[1], Roger Springett[2], Christoph Leussler[3], Peter Mazurkewitz[3], Stephen B. Tuttle[1], Summer L. Gibbs-Strauss[1], Shudong S. Jiang[1], Hamid Dehghani[1,4], Keith D. Paulsen[1]

1. Thayer School of Engineering, Dartmouth College, Hanover, New Hampshire 03755
2. Dartmouth Medical School, Dartmouth College, Hanover, New Hampshire 03755
3. Philips Research Europe, Sector Medical Imaging Systems, Hamburg, Germany
4. School of Physics, University of Exeter, Exeter, UK EX4 4QL
Scott.C.Davis@dartmouth.edu, Brian.W.Pogue@dartmouth.edu

A multi-channel spectrally resolved optical tomography system to image molecular targets in small animals and human breasts from within a clinical MRI is described. Long source/detector fibers operating in contact mode couple light from the tissue surface in the magnet bore to 16 spectrometers, each containing two optical gratings optimized for the near infrared. High sensitivity, low noise CCDs connected to each spectrograph to provide CW detection of the spectrally resolved light. Exposure times are automatically optimized during acquisition. Images of fluorescence yield are recovered using a non-linear reconstruction approach based on the diffusion approximation of photon propagation in tissue, and the tissue morphology derived from the MRI images serves as an imaging template to guide the optical reconstruction algorithms. Sensitivity studies show recovered values of ICG fluorescence yield are linear down to concentrations of 500pM in a 70mm diameter homogeneous phantom. Phantom data also demonstrates imaging capabilities of imperfect fluorophore uptake in tissue volumes of clinically relevant sizes. A unique rodent MR coil provides optical fiber access for simultaneous optical and MR data acquisition of small animals. A pilot small animal study using human gliomas in mouse brains demonstrates the feasibility of imaging an Epidermal Growth Factor Receptor (EGFR) targeted fluorescent probe in vivo using combined optical-MRI information. Though the focus of this paper is fluorescence imaging, the system is capable of MRI-guided spectrally resolved absorption/scatter-based imaging and bioluminescence imaging.

I. INTRODUCTION

Imaging fluorescent molecular targets to characterize tissue pathology in vivo is an important objective with broad implications for drug development in small animals and clinical diagnosis. Given the availability of targeted molecular imaging agents for animal research, several small animal fluorescence tomography scanners have been developed to provide volumetric images of fluorescence activity [1-6]. Imaging larger tissue volumes, such as the human breast, poses additional challenges which include collecting an adequate number of photons to produce meaningful measurements. In addition to the technical challenges, appropriate NIR fluorophores approved for tomographic imaging in humans are scarce. Despite this, a handful of researchers have worked toward developing and assessing DOFT imaging techniques should specific, targeted probes earn clinical approval [7-11]. Fluorescence tomography images of human

1

breast using the non-specific fluorophore indocyanine green (ICG) have only very recently been published [7].

Pursuing non-invasive optical molecular imaging at depth implies that interrogating photons are measured only at the tissue surface, making the image inversion problem severely underdetermined and ill-posed, even with dense source and detector configurations. The highly scattered photon field limits the resolution of DOT images and quantitative interpretation can be difficult. However, researchers have found that using tomographic data acquired at discrete NIR wavelengths and incorporating the spectral features of dominant tissue chromophores in the imaging algorithm improves imaging performance [12-18]. In general, greater quantitative accuracy is expected as the number of wavelengths increases; however, image resolution is still relatively poor compared to many clinical imaging systems. Additional information may be used to guide image recovered by noting that variation in tissue optical properties can be loosely associated with the tissue's anatomical structure, providing an opportunity to incorporate anatomical information from highly-resolved conventional imaging systems in the recovery of optically relevant molecules. In practice, standard MRI images have been used to guide diffusion-based image reconstruction of endogenous tissue chromophores [19-21] and recently of fluorescent molecules [8]. An imaging system that combines fully resolved spectra of transmitted or emitted light and simultaneously acquired MRI data can provide a particularly rich data set for a variety of imaging applications.

This work describes a unique multi-channel spectrometer-based detection system for imaging fluorescence yield in small animals and breast-sized domains. The optical detection system couples directly into a Philips 3T magnet for simultaneous MRI and optical data acquisition. In this configuration, the highly resolved MR images are used as templates for imaging fluorescence yield from emission of an injected fluorophore. A custom-designed and manufactured rodent coil produced by Philips Research, Hamburg integrates the fiber optic array into a small-diameter RF pickup coil for imaging small animals in the 3T MRI. Though the results presented in this paper focus on the system's fluorescence imaging capabilities, it also acquires broadband CW transmission measurements for MRI-guided spectrally constrained reconstruction of chromophore concentrations as well as bioluminescence emission for spectrally resolved MRI-guided bioluminescence tomographic imaging.

II. SYSTEM DESIGN

The parallel spectrometer-based tomographic imaging system, depicted in Fig. 1, couples into a Philips 3T MRI magnet and was developed to acquire spectrally resolved transmission, fluorescence emission, and bioluminescence spectra. Major system components described below include, the spectrograph, detection array, fiber optic transmission of light to and from the tissue surface, the acquisition light source, and MRI coils which integrate the fiber optic patient interface. Photographs of the system are presented in Fig. 2.
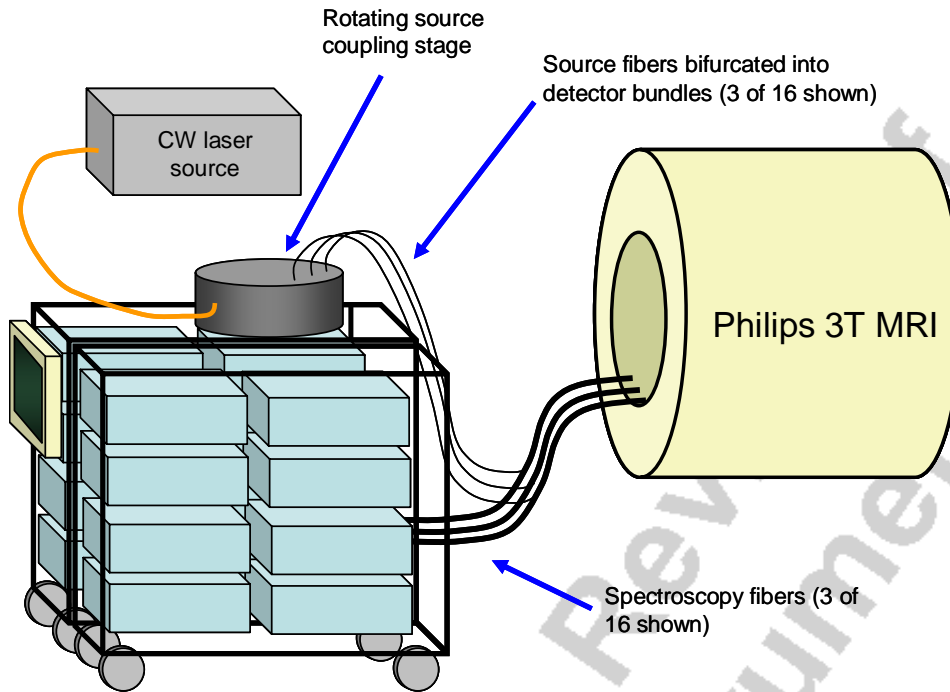
2

Fig. 1. Diagram of the MRI-coupled 16 channel spectroscopy system for fluorescence tomography. Long, bifurcated spectroscopy fibers couple contact mode source-detection directly into the MR bore.

A. Optical Detection System

The optical detection system is composed of 16 Princeton Instruments/Acton Insight:400F Integrated Spectroscopy Systems (Acton, MA) residing in two custom designed wheeled carts (8020, Columbia City, IN). The Insight 400F consists of a 0.3m F3.9 imaging spectrograph and a low noise, front illuminated CCD camera (Pixis 400F) cooled to -70 °C. The 1340 x 400 pixel CCD is binned vertically to maximize detector area/wavelength providing a binned pixel area of 0.16 mm^2. Manufacturer specifications indicate a dark current of 0.0025 electrons/pixel/s and quantum efficiencies of 0.45 at 750 nm and 0.20 at 950 nm. Each spectrograph contains a motorized grating turret holding 300 and 1200 l/mm gratings, which when coupled to the CCD, provide spectral ranges of 60 and 300 nm for a single grating position, respectively. Both gratings are blazed at 750nm for maximum efficiency in the NIR.
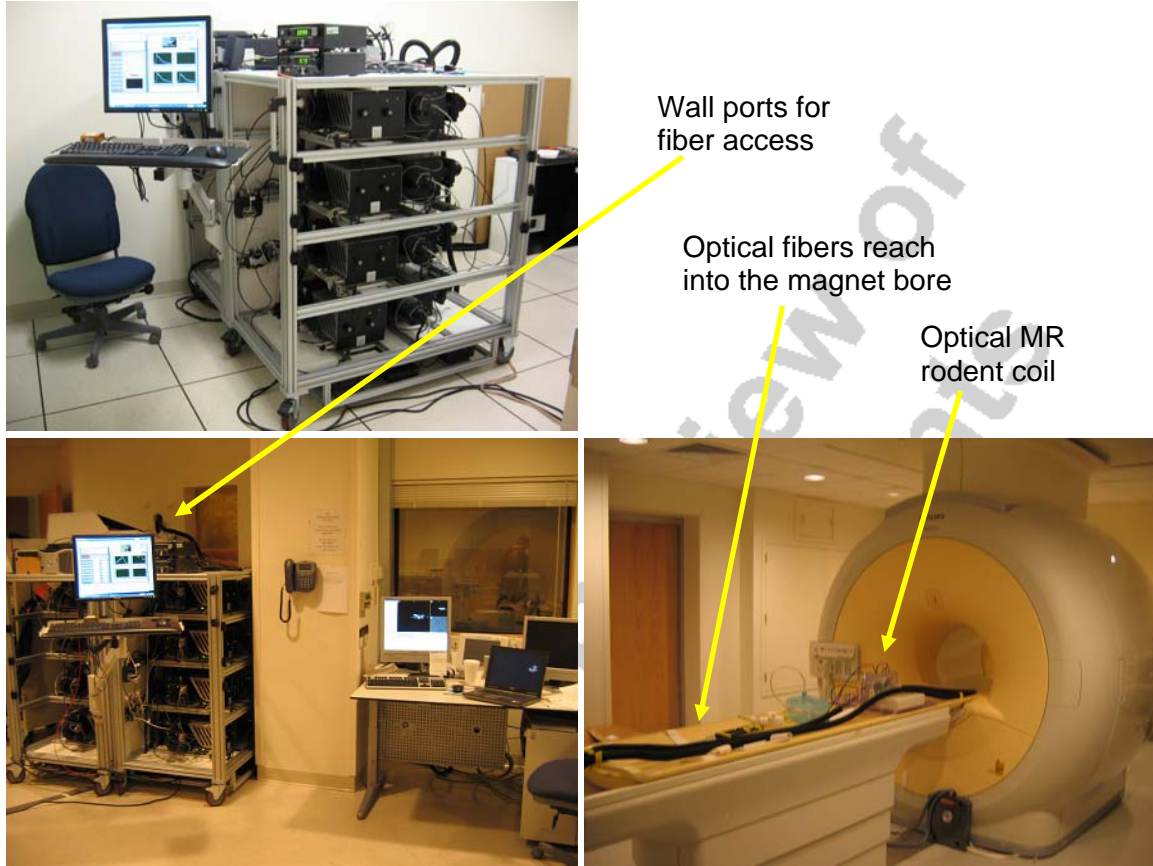
Fig. 2. Top left: The spectroscopy system is built into carts which can be wheeled into the MRI control room (bottom left). Thirteen meter long fiber bundles extend through ports in the wall and directly into the MRI bore (bottom right).

B. Light collection and delivery

Sixteen custom designed bifurcated fiber bundles (Zlight, Latvia) channel light to and from the imaging domain. Each fiber bundle is composed of eight 13 meter long and 400 μm diameter silica fibers which contact the tissue surface. Seven fibers from each bundle connect to the input system of each of the spectrographs while the eighth, known as a source fiber, branches off to the source coupling system. The light source is coupled sequentially into one of the sixteen fibers using a precision rotating stage (Velmex, Bloomfield, NY). This configuration requires no fiber-to-fiber coupling between the tissue surface and the spectrometers and provides parallel detection of full spectra for each source position. The detector associated with the active source fiber is deactivated, resulting in 15 measurements for each 16 source positions, though this may be reduced for smaller domains. Incidentally, the motorized rotating stage unit also contains 15 frequency modulated PMTs in a configuration identical to that described in [22].   This design is part of an ongoing system expansion which will provide multi-wavelength frequency domain transmission mode acquisition through the source branch of the optical fibers and is addressed more thoroughly in the Discussion section of this work.

The detection branch of the fiber bundles are arranged in a line and coupled to the spectrographs via custom designed input optics mounted on each spectrograph as depicted in Fig. 3. An F1.4, 25mm focal length digital camera lens (MegaPixel, Edmund Optics, Barrington, NJ) collects and collimates almost the full cone of light emitted from

the detector fibers (NA = 0.37). The collimated light passes through a fully automated 6-position filter wheel containing two long pass interference filters, one 650 nm and the other 720 nm cutoffs (Omega, Brattleboro, VT), for fluorescence emission acquisition as well as 1 OD and 2 OD neutral density filters (Thorlabs, Newton, NJ) which increase the dynamic range of transmission imaging by about 2 OD. Filter wheel positions are automatically adjusted during image acquisition depending on the type of acquisition. A 25mm diameter, 60mm focal length NIR achromat (Thorlabs, Newton, NJ) focuses the collimated and filtered light onto the input slit. The F# matching of fiber to spectrograph utilizes the high NA of the fibers to minimize the number of fibers in the bundle. The spectrograph entrance slits are opened fully to maximize photon collection and the magnified image of the fiber array at the slit plane defines an effective slit width of just over 1mm so that the system operates at a resolution of about 2.2 and 11.2nm using the 1200 and 300 l/mm grating respectively. The spectral resolution can be increased at the cost of throughput by reducing the input slit width.
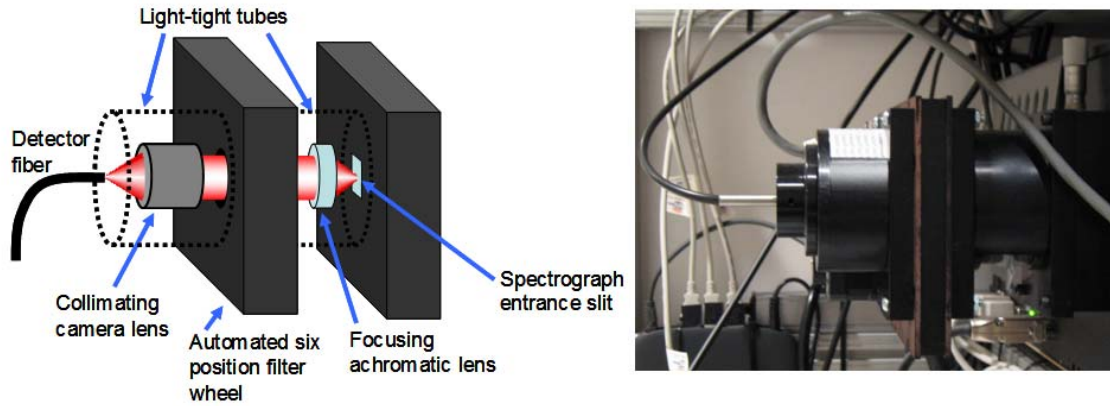

Fig. 3. Diagram (top) and photograph (bottom) of the custom designed entrance optics. Lenses collimate the incoming light for filtering with selectable interference or ND filters and focus the light onto the spectrometer.

C. Light sources

The imaging method for a given acquisition determines which light source to incorporate into the imaging sequence. Currently available sources include a high power tungsten white light source for broadband transmission tomography, a variety of laser diodes for transmission and fluorescence imaging, and a high power Mai Tai Ti:Sapphire laser (Spectra Physics, Irvine, CA) capable of automated wavelength tuning between 690 and 1020 nm. Bioluminescence mode imaging requires no external source. Since the focus of the work presented here is fluorescence imaging, data for the presented examples was acquired using a 690 nm CW laser diode (Applied Optronics, South Plainfield, NJ) to excite the fluorophore.

D. Patient/animal interface

A unique MRI rodent coil designed in collaboration with Philips Research Europe (Hamburg, Germany) features sixteen access holes and nylon set screws to accommodate the spectroscopy fibers in a circular array. While small magnet bore animal systems are restricted to birdcage coil configurations, larger bore commercial clinical MR scanners

allow the use of solenoid coil designs. The B1-field direction of this coil must be oriented orthogonal to the main Bo field axis. For small animal imaging at 3T, the solenoid coil provides high B1 sensitivity and good field of view coverage. Calculations of electromagnetic field and coil characteristics were performed from simulations using a commercially available EM program (FEKO), which is based on the method of moments (Fig. 4).

The solenoid coil has an open inner diameter of 70mm and is built from 8mm wide strip conductors wound around a fiberglass cylinder. The coil support cylinder is made of glass fiber and is mechanically fixed to a side wall. The parallel windings are connected as shown in Fig. 5 and the gap between individual strip conductors is 8mm, providing ample space to accommodate the spectroscopy fibers. Circumscribing the fiberglass coil support cylinder is a removable polycarbonate cylinder containing nylon set screws to affix the spectroscopy fibers.
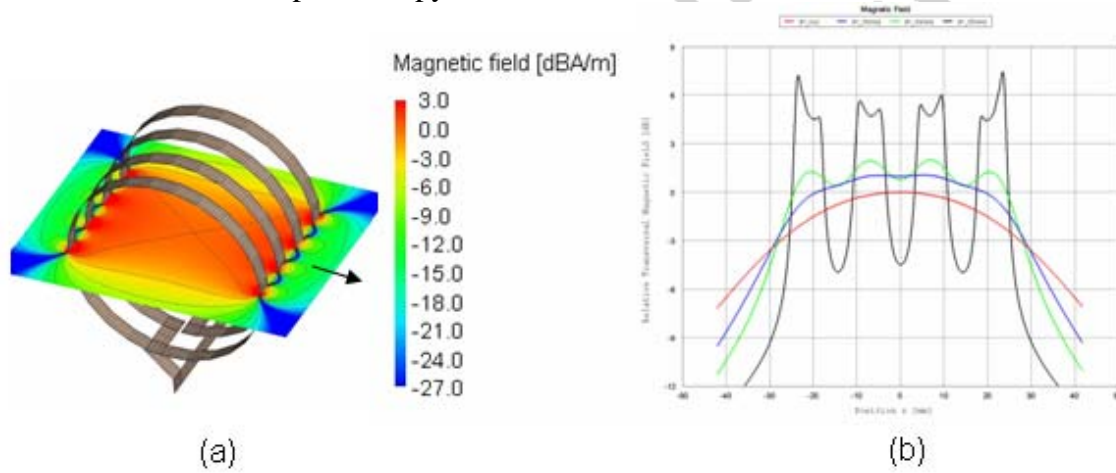

Fig. 4. (a) Relative transversal magnetic field of the solenoid coil. The isocenter is set to 0dB and the arrow shows the B0 direction. (b) Sensitivity profiles along the coil axis (perpendicular to the main field B0) for different distances from the isocentre.

The overall inductance of the solenoid is Ls=1,024μH at 127MHz. Sixteen equidistant splits with non magnetic capacitors (ATC 100B) are introduced along the conductor to avoid current inhomogeneities (propagation effects). During the transmit phase, the coil is detuned by 3 independent parallel detuning circuits distributed along the solenoid, which make the coil transparent for the B1 transmit field. Optimized blocking radio frequency (RF) chokes prevent RF leakage and provide a high Q factor measured at $Q_L = 600$ for the unloaded coil. A low noise preamplifier is connected directly to the solenoid and optimal noise matching is performed via a low loss pi network.

(a)   (b)

Fig. 5. (a) Photograph of the coil layout showing connected strip conductors and holes to provide access for optical fibers. The custom designed mouse bed accommodates the spectroscopy fiber bundles and fits into the rodent coil for simultaneous MR and optical acquisition (b).

For mouse brain imaging, a custom designed molded mouse bed, also shown in Fig. 5, contains fiber optic access holes to provide stable positioning of eight spectroscopy fibers around the mouse head, reducing the data set to a maximum of 56 source-detector pairs.

Larger volumes and patient breast imaging capabilities are provided by a fiber optic ring attached to a commercial 3T MRI breast coil (MRI Devices, Waukesha, WI), depicted in Fig. 6. The current design requires manual fiber positioning using set screws, however, spiral ring and parallel plate geometries may be implemented for more reliable positioning.

Fig. 6. The patient interface is a circular array of fibers that couples into a standard MR breast coil (a), though parallel plate geometries are also under consideration (b).

E. Automated Acquisition

The system is operated using a Dell desktop PC running Windows XP Professional. Image acquisition is automated using custom programs written in Labview (National Instruments, Austin, TX) developed with the SIToolkit camera/spectrometer drivers produced by Rcubed, LLC (Lawrenceville, New Jersey). USB cables connect all camera/spectrometer/filter wheel units to the computer, and the motorized source-coupling stage is connected via a serial cable. A screenshot of the primary acquisition control program is depicted in Fig. 7. The user interface is designed to minimize

technician training. Imaging modes include Fluorescence Tomography, Transmission Tomography, Bioluminescence Tomography, Raw Data Only, System Calibration, and Basis Spectra Acquisition, and once a mode is selected, only relevant options pertaining to that imaging mode appear on the screen. Exposure times may be set manually by the user or automatically determined using an optimization routine which performs test exposures to calculate ideal exposure times for image acquisition. Additional options include real-time spectrum calibration and spectral fitting and automatic neutral density filtering to preferentially decrease filter OD as a function of source-detector distance for non-fluorescence measurements.
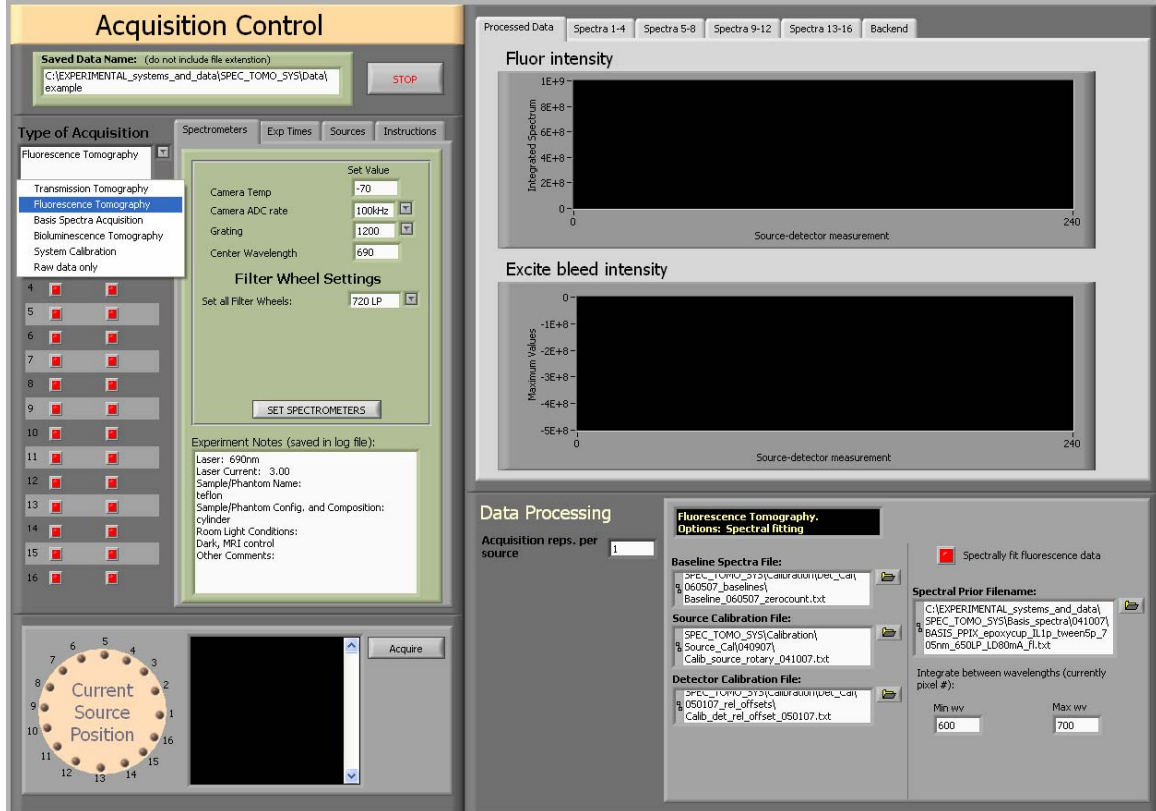

Fig. 7. Front panel of the spectroscopy system's image acquisition program.

III. FLUORESCENCE TOMOGRAPHY IMAGE FORMATION

The MRI-guided FEM image reconstruction implementation is described extensively in Ref [8]. In general, the approach used here is:

1) Acquire frequency domain data (PMT detection system) at the excitation wavelength and use this data to reconstruct for optical properties, μ_{ax} and μ_{sx}',

2) Acquire frequency domain data (PMT detection system) at the emission wavelength and use this data to reconstruct for optical properties, μ_{am} and μ_{sm}',

3) Acquire CW transmission data using the fluorescence excitation laser source and the spectrometer detection system.

4) Acquire CW fluorescence emission data, calibrate this data using the data acquired in part (3), and use the reconstructed optical properties to recover

8

fluorescence yield, a product of the fluorophore's quantum efficiency, η, and its absorption coefficient, $\mu_{af}(r)$.

Currently, frequency domain data required for parts (1) and (2) is collected using a separate DOT imaging system used in clinical exams and described in Ref[22]. PMT-based frequency domain capabilities are being integrated into the spectrometer system carts to provide frequency domain and CW spectroscopic detection in a single system. These modifications are outlined in the Discussion section.

MRI images acquired simultaneously with optical data are used to generate the finite element domain for optical tomography image recovery. MR images are segmented using thresholding, region growing, and manual image manipulation in Materialize Mimics software (Ann Arbor, MI). Source/detector fiber optic positions are registered with reference to MR sensitive fiducials attached to the patient or animal fiber interface. Exported mask files are used to generate FEM meshes compatible with the optical tomography modeling and image reconstruction software described in Ref[8].

Two methods are used to incorporate tissue structural information derived from simultaneously acquired MR images into the optical tomography reconstruction algorithm. One approach structures the inverse regularization matrix based on segmented MR images, known as a "soft" priors approach since each node updates independently, allowing the recovery of tumor regions not explicitly segmented from the MR image. Alternatively, the "hard priors" approach homogenizes each segmented region and is therefore unyielding in its application of spatial guidance[23,24].

In the soft priors approach, spatial prior information is incorporated by assuming a 'generalized Tikhonov' penalty term that results in a Laplacian-type regularization matrix. The computational approach is to minimize the difference between measured fluence, Φ^{Meas}, at the tissue surface and calculated data, Φ^C. The iterative update equation for the optical properties $\mu = (\mu_a, \kappa)$, where μ_a is the absorption coefficient, κ is the diffusion coefficient, $\kappa = 1/3(\mu_a + \mu_s')$, and μ_s' is the diffusion coefficient, pertains to steps (1) and (2) above and is given by

$$\Delta\mu_{x,m} = \left[J^T J + \beta_{x,m} L^T L\right]^{-1} J^T \left(\Phi_{x,trans\_m}^{Meas} - \Phi_{x,trans\_m}^{C}\right) \qquad (1)$$

for the excitation and emission wavelengths x and m. Once these values are know, the fluorescence yield update can be calculated,

$$\Delta\eta\mu_{af} = \left[J^T J + \beta_f L^T L\right]^{-1} J^T \left(\Phi_m^{Meas} - \Phi_m^{C}\right) \qquad (2)$$

where in both update equations, J is the Jacobian matrix describing the sensitivity of boundary data to the parameter of interest, and β is a fixed fraction multiplied by the maximum value on the diagonal of $J^T J$. Spatial prior information is introduced in the dimensionless 'filter' matrix, L, generated using MRI images segmented into appropriate regions. In this application, each node in the FEM mesh is labeled according to the region, or tissue type, with which it is associated in the MR image.

The hard priors approach applies stricter constraints than the regularization-based implementation described previously. Nodal values are locked together by implicitly

assuming segmented regions in the imaging domain are homogeneous. In practice, the Jacobian matrix is calculated on a fully resolved mesh at each iteration, but then collapsed into segmented regions for the inversion process. This drastically reduces the update parameter space from the product of number of nodes and number of unknown properties to the product of number of regions and number of unknown properties. Confidence in the segmentation is critical since regions are offered no spatial latitude. Indeed, the hard-priors approach is strictly a characterization-based implementation incapable of detection or uncovering false negatives, and therefore does not present as an image recovery problem per se.

IV. OPTICAL DATA PROCESSING

The following outlines the data processing procedure for all optical data collected on the spectroscopy system (A through C) as well as additional calibration procedures for fluorescence emission measurements (D).

A. Baseline/dark current correction

Each CCD displays a baseline offset for zero second acquisitions which must be subtracted from the raw spectra. Multiple repetitions of the baseline offset spectra were measured directly for each spectrometer. The median of the repetitions yields the baseline offset spectra to be subtracted, pixel-by-pixel (assuming vertical binning of the CCD chip), from each acquired spectrum. This is done for each spectrometer.

A similar method was used to correct for the dark current of the CCDs. Dark room acquisitions were recorded for a range of exposure times. Measured counts are proportional to exposure time. The counts per exposure time slope was determined per binned pixel for each spectrometer and is used to subtract dark current from recorded spectra. After baseline and dark current correction, spectra are converted to counts per second.

B. Detector calibration

A first order correction is applied to account for heterogeneity in throughput and wavelength dependence for all optical components between the tissue and CCD detector (ie. detection fibers, input optics, spectrometer optics, and CCD response). Detectors are arranged to circumscribe a 6 cm diameter cylindrical Teflon phantom. An SMA connector is attached to one end of the homogeneous phantom and white light from a high power tungsten white light source is focused into a fiber connected to the centrally located SMA connector. Spectra are recorded with all spectrometers (usually ten repetitions) and inter-detector calibration factors are calculated for every vertical pixel bin (total of 1340) for each spectrometer. This is done for each grating and grating position to be used in image acquisition. Calibration factors are stored and used to scale detected signal in a wavelength dependent manner. This helps reduce the influence of inhomogeneities in the CCD array and partially accounts for throughput variability between detector channels.

A similar approach is used to correct for OD filtering. Since the ND filters have a wavelength dependent response, OD values for every filter are determined experimentally using the spectroscopy system. For a given spectrometer, these values are

calculated for each CCD pixel (vertically binned) for each grating/wavelength range selection. In this manner, a calibration file for a given filter setting at a given grating and wavelength setting will contain 1340 X 16 values of optical density, accounting for number of pixels by number of spectrometers.

C. Source calibration

A first order inter-fiber source strength calibration is recorded by positioning a detector at the radial center of the Teflon cylinder described above. The detected signal from all 16 source fiber positions is then used to determine source scaling factors for future acquisition.

D. Fluorescence emission spectral fitting and data-model calibration

Fluorescence emission light is initially decoupled from the often much more intense excitation signal using long pass interference filters (between 5 and 7 OD depending on the filter set) and the wavelength selectivity of the spectrograph grating. Even with these components in place, light reaching the CCD retains residual signal not associated with fluorescence emission from the fluorophore target, which can be a significant component of the total signal, especially for cases in which the fluorophore has a low quantum yield or is at a low concentrations in the tissue. In order to decouple the true fluorescence signals further, previously recorded "basis spectra" of the residual non-fluorophore originating signal and the pure fluorescence signal are fit to the data. Each spectrograph is used to record its own fluorescence emission basis spectra and residual excitation basis spectra in a controlled manner. All spectra are normalized to the maximum value. Fitting is accomplished by a linear least squares algorithm that minimizes the summation

$$S = \sum_{i=1}^{N} [y_i - (aF(\lambda_i) + bG(\lambda_i))]^2 \tag{3}$$

with respect to a and b, where y_i is the measured intensity at a given wavelength pixel, F and G are the residual excitation and fluorescence basis spectra, a and b are the coefficients recovered in the minimization procedure, and N is the number of wavelength pixels per spectrum. The algorithm determines the amount of fluorescence emission and excitation crosstalk in the measured spectrum, the sum of which best fits the data in a least squares sense. This procedure is applied to each recorded fluorescence spectrum, a total of 240 spectra for a given acquisition. The spectral fitting procedure is demonstrated for two different ICG concentrations in a homogeneous phantom in Fig. 8. In some cases, the fluorescence peak has been observed to shift to longer wavelengths in large phantom volumes. To account for this, the minimization may incorporate the position of the peak as a free parameter. The resulting fluorescence emission peak is integrated to provide a single fluorescence intensity measurement for a given source-detector pair.
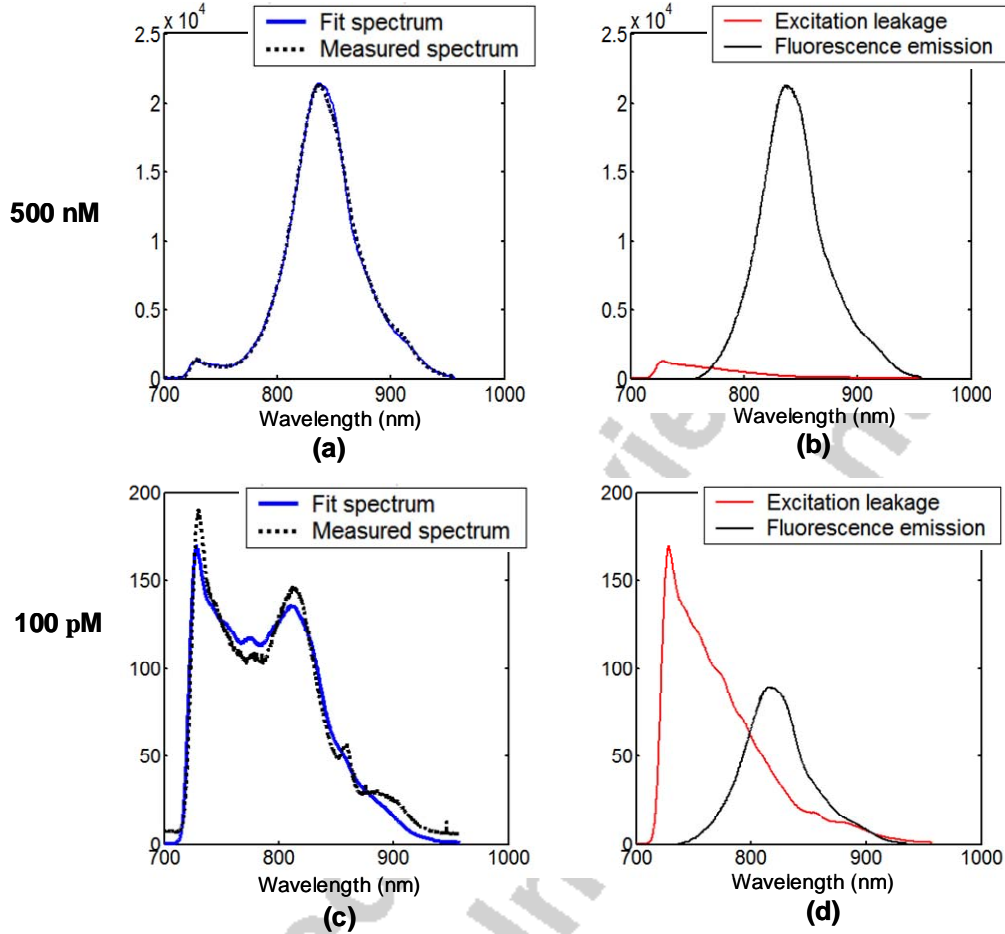
Fig. 8. A spectral fitting routine is used to decouple fluorescence spectra from the measured signal. The spectral fitting algorithm determines the relative contribution of the basis spectra (right column, (b) and (d)) which best fits the measured spectrum. Two examples are presented above, both for a 70mm diameter homogeneous phantom containing intralipid, ink and ICG (500nM for graphs (a) and (b) and 100pM for graphs (c) and (d)).

Integrated fluorescence emission measurements are calibrated using the integrated transmission measurements acquired using the spectrometer system and the optical parameter images from the frequency domain acquisition to scale the fluorescence data to the system model in the following manner,

$$\Phi_{fl_i}^{calib} = \Phi_{fl_i}^{meas} \frac{\Phi_{x_i}^{model}}{\Phi_{x_i}^{meas\_spec}} \tag{4}$$

where the index i indicates a single data point or source-detector pair. Φ_{x}^{model} is the intensity boundary data calculated from the images of μ_{ax} and μ_{sx}' recovered using the frequency domain measurements from the PMT clinical system. This calculated, or "model", boundary data must correspond to the spectrometer fiber positions, which do not necessarily have to be identical to those used in the frequency domain system. The

quotient in Eq. 4 essentially provides a scaling factor for the fluorescence measurements which accurately scales the fluorescence data to the FEM model and accounts for inter-detection channel throughput and fiber coupling discrepancies. An initial estimate for the iterative reconstruction algorithm is determined using a homogeneous fitting routine. This procedure uses the bisection method to minimize the data-model misfit assuming a homogeneous distribution of fluorescence yield.

V. SYSTEM PERFORMANCE

A. Repeatability

A 8.6cm diameter homogeneous phantom composed of silicone, titanium dioxide, and India ink was used to measure the repeatability of transmission mode measurements using the spectroscopy system. Optical properties of the phantom were approximately 0.004 mm^{-1} and 1.91 mm^{-1} for the absorption and reduced scattering coefficients respectively. Measurements were repeated at each source-detector position using the 690 CW laser source. For a single vertically binned pixel array, the average and maximum standard errors at the laser peak are 1.4% and 1.8%, respectively, if fiber positions were not changed in between measurements. These increase to 18.3% and 19.5% with fiber repositioning, indicating that fiber coupling is the most significant source of error. If pixels are binned throughout the laser peak, the average and maximum standard errors change to 0.28% and 0.37% for fibers remaining in contact with the phantom and 14.8% and 16.3% for re-positioned fibers.

Determining measurement repeatability in fluorescence mode is less straightforward given the signal dependence on fluorophore concentration, absorption spectrum, and quantum yield. For this study, a 70 mm diameter liquid phantom containing DPBS, 1% intralipid, India ink, and 10nM ICG was used to determine measurement repeatability. This measure was calculated in two ways, one considered only the raw data for a given binned pixel array and resulted in a mean standard error of 0.7% and maximum standard error of 1.4% for the pixel array at the fluorescence peak. The second measure was determined based on the integrated intensity from the full calibration and spectral fitting routine, resulting in an average standard error of 0.6% and maximum standard error of 1.8%. It is clear that fiber positioning variability would dominate the data error for fluorescence measurements in this case. However, fluorescence measurements offer a unique opportunity to account for fiber coupling variability. This is accomplished by calibrating the fluorescence measurements to the transmission measurements in the same geometry, as described in Section IV, (D).

B. Sensitivity

A 70 mm diameter liquid phantom containing DPBS, 1% intralipid and India ink was used to investigate the overall sensitivity of the system to ICG fluorescence. ICG dye dissolved in DI water was added to the solution to obtain solutions ranging from 10 pM to 1 μM ICG. The optical properties, μ_a and μ_s' were determined for each concentration from data collected using the clinical frequency domain system. Since the domain was known to be homogeneous, these properties were determined in a homogeneous fitting procedure only.

13

Fluorescence emission and excitation transmission measurements were recorded for each phantom, with a maximum allowed camera integration time of 120 seconds applied to the fluorescence measurements. Calibrated fluorescence intensity measurements were used to calculate homogeneous values of fluorescence yield. These values are plotted as a function of known ICG concentration in Fig. 9.
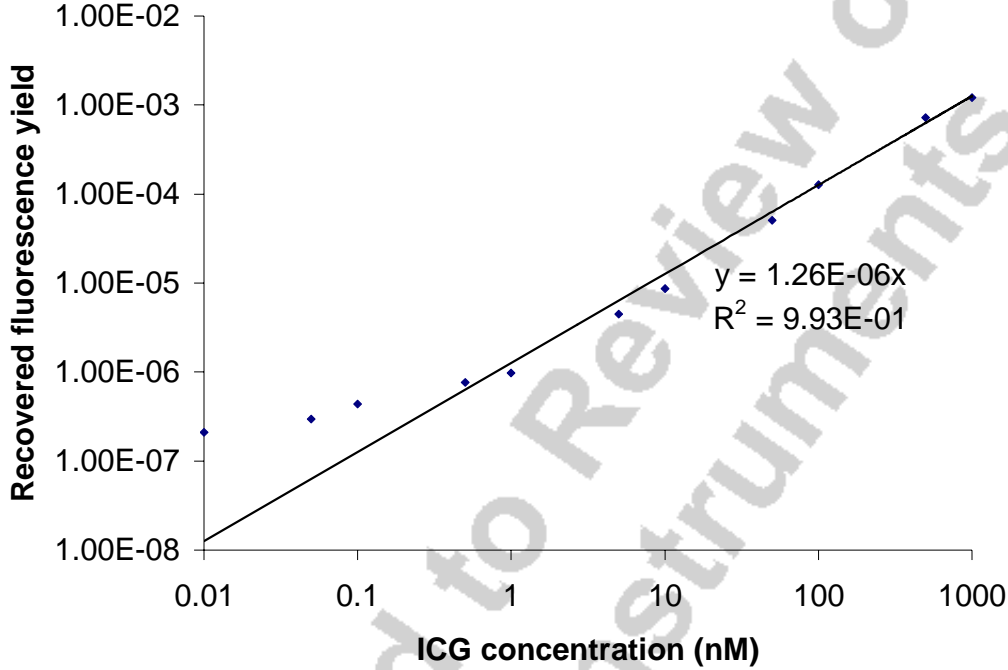

Fig. 9. Recovered values of fluorescence yield as a function of ICG concentration in a 70mm liquid phantom. Values were determined using a homogeneous fitting algorithm for the background optical properties as well as the fluorescence yield.

The y-intercept was forced to zero for the linear fit. Recovered values are linear with values of known concentration with an R^2 value of 0.99. Since fluorophore quantum yield is not explicitly known in this solution, the calculated slope of the line does not provide information on the actual relationship between true and recovered concentration. Below 500 pM, the recovered values of fluorescence yield depart from the trend observed for higher concentrations. This may indicate that the noise floor has been reached, or that there is a system bias which may be corrected.

C. Phantom imaging

A heterogeneous liquid phantom was used to demonstrate imaging large volumes with imperfect tumor-to-background uptake. The phantom was composed of DPBS, 1% intralipid and India ink, resulting in background optical properties of $\mu_a = 0.005$ mm^{-1} and $\mu_s' = 1.4$ mm^{-1}. ICG dissolved in DI water was added to the phantom volume to obtain a 300 nM ICG solution. A thin-walled plastic cylinder was positioned between the edge and center of the phantom to simulate a 2 cm diameter tumor region. The inclusion consisted of the same solution found in the phantom background, though the ICG concentration was elevated to 1 μM, providing a total contrast of just over 3.3:1. Background optical properties were determined by imaging the phantom in a separate

frequency domain clinical system and values for 785nm were used for this experiment. The spectroscopy system was then used to acquire excitation intensity and fluorescence emission measurements. Integrated intensities were calibrated to the model as described earlier and images were reconstructed using an algorithm without spatial guidance as well as the soft spatial priors implementation. The resulting images are shown in Fig. 10. Tumor-to-background contrast can be deciphered in both images, however, the spatially guided implementation provides a more accurate representation of the imaged domain. Inclusion borders are more clearly defined and the image represents substantially higher tumor-to-background contrast.
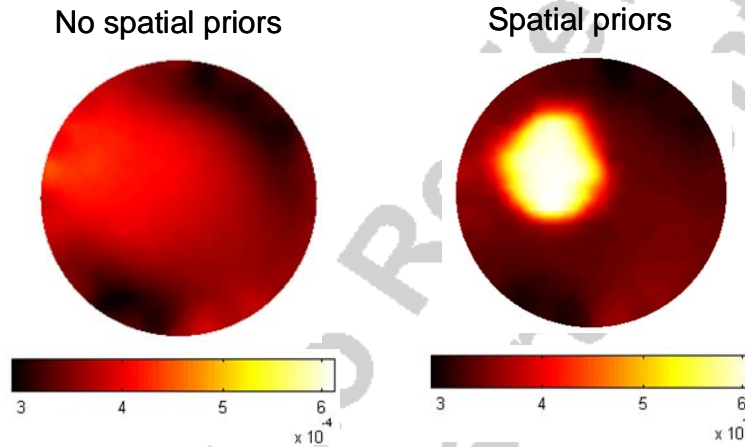

Fig. 10. Images of fluorescence yield for a 70mm diameter liquid phantom containing an ICG heterogeneity. Target-to-background concentration of ICG was 3.3:1. Images reconstructed using spatial soft priors, depicted in (b), are more accurate qualitatively and in terms of recovered contrast than images recovered without the spatial priors implementation (a).

D. Small animal imaging

An animal pilot study demonstrates the ability of the system to image an EGFR targeted fluorescent probe in mouse brain tumors. U-251 human glioma tumors were implanted intracranially in male nude mice 19 days prior to the imaging study. Simultaneous gadolinium enhanced T1 MRI and fluorescence tomography acquisition of the population was completed prior to IRDye[®] 800CW EGF Optical Probe (LI-COR Biosciences, Lincoln, NE) IV administration (1 nM) and at 24 hour intervals after injection over the course of 72 hours. Eight fibers were used in this study and fiber-tissue contact positions were determined in reference to MR sensitive fiducials on the molded mouse bed. For each imaging session, a single coronal slice was segmented into regions using Materialize Mimics software. The example in Fig. 11 shows an MR coronal slice of the tumor-visible mouse 48 hours after IRDye[®] 800CW EGF Optical Probe administration and the resulting MR segmentation. The regionized mask was exported as a bitmap file from which a two dimensional mesh was generated for fluorescence reconstruction.
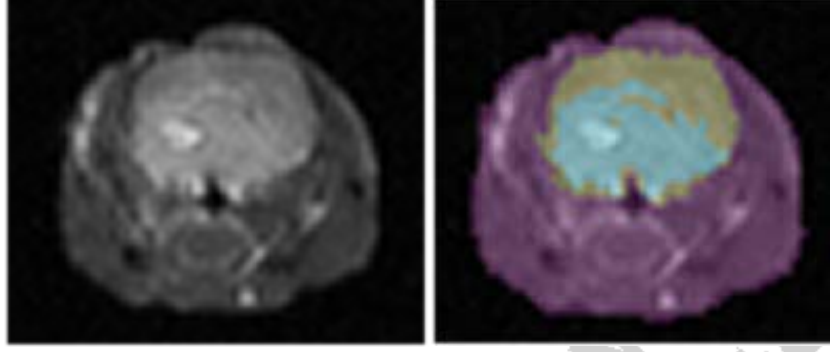
Fig. 11. The coronal slice from Gadolinium enhanced T1-weighted images of a tumor bearing mouse brain (left) is segmented into three regions using MIMICS software. The segmented image is used to generate an FEM mesh for spatially-guided fluorescence reconstruction.

The spectral fitting technique described in section IV, (D) was used to generate integrated intensity values of fluorescence emission from basis spectra of EGF Optical Probe fluorescence. Reconstructed images with and without the use of hard spatial priors are presented in Fig. 12. Recovered values of fluorescence yield are highly surface weighted and well outside the tumor region when spatial priors are not used while the hard priors implementation shows elevated levels of fluorescent activity in the tumor region. Analysis for the remaining population and imaging times is ongoing. An important test will be how the hard-priors implementation handles false positives in healthy regions, and non-tumor bearing mice, introduced by incorrect MR segmentation.
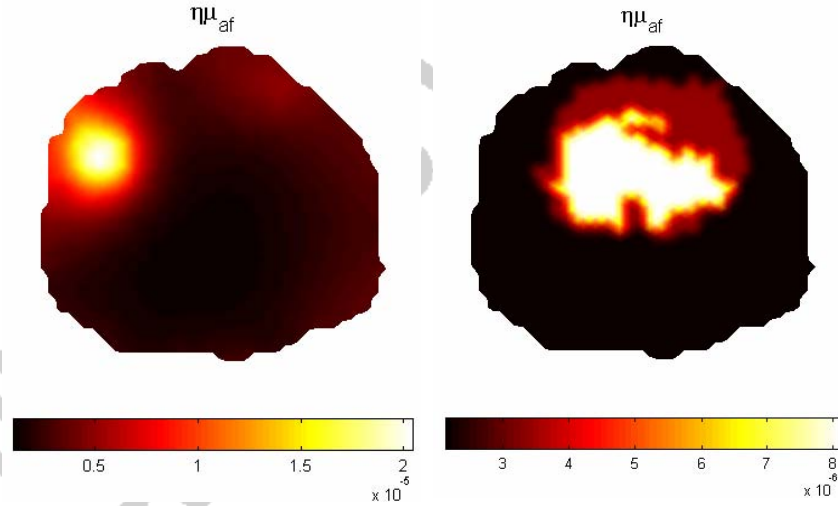

Fig. 12. Reconstructed images of fluorescence yield for a tumor-bearing mouse using only the outer boundary for spatial priors (left) and using spatial hard priors (right).

VI. DISCUSSION

An MRI-coupled optical tomography system has been developed to image fluorescence yield in a variety of tissue volumes. A unique rodent coil developed specifically for this system provides high resolution MRI images of small animals. Through a variety of spatial prior implementations, these images provide the imaging

16

template upon which the fluorescence activity is reconstructed. The system's high sensitivity, low noise CCD detectors were shown to be stable and provide repeatable measurements, the most significant error originating from fiber coupling errors. Fluorescence emission intensity may be scaled to the excitation laser transmitted intensity to account for these errors.

Characterizing the system's sensitivity to fluorophore is complex given the dependence on fluorophore concentration, absorption spectra, excitation filtering, and quantum yield. Sensitivity results of a commonly used fluorophore in a reasonably sized phantom are presented and demonstrate a linear response of the fluorescence yield fit to fluorophore concentration down to 500pM concentrations. Below this concentration, the system appears to have reached the noise floor, though this may also be a system bias which may be accounted for in future work.

Preliminary imaging studies demonstrate an ability to image relatively low fluorescence contrast (3.3 : 1) in relatively large tissue volumes (70 mm diameter), contingent upon the availability of spatial prior information provided by the MRI. Additionally, it was also shown that imaging a targeted fluorophore in mouse gliomas is feasible and benefits dramatically from the structural information. A larger mouse population study is currently underway to further characterize in vivo imaging performance in small animals.

The work presented here required the use of a separate frequency domain imaging system to obtain background optical properties and calibrate the fluorescence data to the algorithmic model. This is inconvenient at best and limits many of the advantages of the MRI-coupled imaging system. Importantly, the lack of FD imaging capabilities integrated into the imaging system, background optical properties may not be acquired without re-positioning the subject. Integrating PMT-based frequency domain detection into the spectroscopy system is underway. The rotating stage was constructed with 15 PMT detectors in a design identical to that reported in [22]. In this configuration, the source branch of the spectroscopy fibers will serve as both light delivery and pickup channels for the PMT's. These components are already in place and undergoing calibration. It is possible that the source fiber diameter is too small to collect enough light to image through larger tissue volumes, though this may be addressed by integrating larger fibers into the array. Available light sources for the FD system include six laser diodes of different wavelengths such as used in our legacy systems, or a Ti:Sapphire laser system which uses the repetition pulse rate to provide the modulation frequency of the FD measurement, described in Ref[25].

This unique system provides rich spectral information in a variety of diffuse optical imaging modes including broadband NIR transmission, fluorescence and bioluminescence. In fluorescence mode, the spectrograph system provides several advantages over filtered intensity measurements. Spectrally resolved detection provides exceptional wavelength selectivity for excitation filtering. The system may also be used to acquire emission data from multiple fluorophores simultaneously, contingent upon the individual fluorescence peaks being resolved well enough for the spectral fitting technique to extract the contribution from each fluorophore. Finally, if the excitation contamination can be suppressed dramatically, the spectrally resolved emission spectra may be used to improve localization and quantification of the fluorescence activity. This technique, which accounts for the wavelength depended absorption of the emission peak

as it propagates through the tissue volume, would be similar to the spectrally resolved approach used in bioluminescence tomography and is under development.

1   N. Deliolanis, T. Lasser, D. Hyde, A. Soubret, J. Ripoll, and V. Ntziachristos, Optics Letters **32,** 382-384 (2007).

2   H. Meyer, A. Garofalakis, G. Zacharakis, S. Psycharakis, C. Mamalaki, D. Kioussis, E. N. Economou, V. Ntziachristos, and J. Ripoll, Applied Optics **46,** 3617-3627 (2007).

3   S. V. Patwardhan, S. R. Bloch, S. Achilefu, and J. P. Culver, Opt. Exp. **13,** 2564-2577 (2005).

4   J. Ripoll, R. B. Schulz, and V. Ntziachristos, Physical Review Letters **91,** 5 (2003).

5   R. B. Schulz, J. Ripoll, and V. Ntziachristos, IEEE Transactions on Medical Imaging **23,** 492-500 (2004).

6   G. Zacharakis, J. Ripoll, R. Weissleder, and V. Ntziachristos, IEEE Transactions on Medical Imaging **24,** 878-885 (2005).

7   A. Corlu, R. Choe, T. Durduran, M. A. Rosen, M. Schweiger, S. R. Arridge, M. D. Schnall, and A. G. Yodh, Optics Express **15,** 6696-6716 (2007).

8   S. C. Davis, H. Dehghani, J. Wang, S. Jiang, B. W. Pogue, and K. D. Paulsen, Optics Express **15,** 4066-4082 (2007).

9   A. Godavarty, M. J. Eppstein, C. Zhang, and E. M. Sevick-Muraca, Radiol. **235,** 148-54 (2005).

10   A. Godavarty, A. B. Thompson, R. Roy, M. Gurfinkel, M. J. Eppstein, C. Zhang, and E. M. Sevick-Muraca, J. Biomed. Opt. **9,** 488-96 (2004).

11   A. Godavarty, C. Zhang, M. J. Eppstein, and E. M. Sevick-Muraca, Med. Phys. **31,** 183-90 (2004).

12   R. Choe, A. Corlu, K. Lee, T. Durduran, S. D. Konecky, M. Grosicka-Koptyra, S. R. Arridge, B. J. Czerniecki, D. L. Faker, B. Chance, M. A. Rosen, and A. Yodh, Med. Phys. **32,** 1128-1139 (2005).

13   A. Corlu, R. Choe, T. Durduran, K. Lee, M. Schweiger, S. R. Arridge, E. M. Hillman, and A. Yodh, Appl. Opt. **44,** 2082-2093 (2005).

14   A. Corlu, T. Durduran, R. Choe, M. Schweiger, E. M. Hillman, S. R. Arridge, and A. G. Yodh, Optics Letters **28,** 2339-2341 (2003).

15   A. Li, Q. Zhang, J. Culver, E. Miller, and D. Boas, Optics Letters **29,** 256-258 (2004).

16   S. Srinivasan, B. W. Pogue, B. Brooksby, S. Jiang, H. Dehghani, C. Kogel, W. A. Wells, S. P. Poplack, and K. D. Paulsen, Technology in Cancer Research and Treatment **4,** 513-526 (2005).

17   S. Srinivasan, B. W. Pogue, S. Jiang, H. Dehghani, C. Kogel, S. Soho, J. J. Gibson, T. D. Tosteson, S. P. Poplack, and K. D. Paulsen, Acad. Radiol. **13,** 195-202 (2006).

18   S. Srinivasan, B. W. Pogue, S. Jiang, H. Dehghani, and K. D. Paulsen, Appl. Opt. **44,** 1858-1869 (2005).
19   B. Brooksby, S. Jiang, C. Kogel, M. Doyley, H. Dehghani, J. B. Weaver, S. P. Poplack, B. W. Pogue, and K. D. Paulsen, Rev. Sci. Instrum. **75,** 5262-5270 (2004).
20   M. Guven, B. Yazici, X. Intes, and B. Chance, Phys. Med. Biol. **50,** 2837-2858 (2005).
21   X. Intes, C. Maloux, M. Guven, B. Yazici, and B. Chance, Phys. Med. Biol. **49,** N155-N163 (2004).
22   T. O. McBride, B. W. Pogue, S. Jiang, U. L. Osterberg, and K. D. Paulsen, Rev. Sci. Instr. **72,** 1817-1824 (2001).
23   H. Dehghani, B. W. Pogue, S. Jiang, B. Brooksby, and K. D. Paulsen, Appl. Opt. **42,** 3117-3128 (2003).
24   M. Schweiger and S. R. Arridge, Phys. Med. Biol. **44,** 2703-2722 (1999).
25   J. Wang, S. C. Davis, S. Srinivasan, S. Jiang, B. W. Pogue, and K. D. Paulsen, Journal of Biomedical Optics (2007).